PHYSICAL REVIEW B **106**, 014501 (2022)

Electronic structure and spin-lattice relaxation in superconducting vortex states on the kagome lattice near van Hove filling

Hong-Min Jiang,[1,*] Shun-Li Yu,[2,†] and Xiao-Yin Pan[3,‡]
[1] *School of Science, Zhejiang University of Science and Technology, Hangzhou 310023, China*
[2] *School of Physics, National Laboratory of Solid State Microstructures, Nanjing University, Nanjing 210093, China*
[3] *Department of Physics, Ningbo University, Ningbo 315211,China*

(Received 13 February 2022; revised 17 June 2022; accepted 22 June 2022; published 1 July 2022)

Starting from a tight-binding model on the kagome lattice near the van Hove filling, the superconducting (SC) properties are investigated self-consistently by using the Bogoliubov–de Gennes equations with the consideration of the inequivalent third-neighbor (TN) bonds. Near the van Hove filling, the most favorable SC pairings are found to derive from the electrons belonging to the same sublattice sites, including the on-site *s*-wave and the spin-singlet/spin-triplet TN pairings. The inequivalent TN bonds will result in multiple SC components with different orbital angular momenta for the TN SC pairings. Whereas the density of states and the temperature (T) dependence of the spin-lattice relaxation rate (T_1^{-1}) exhibit distinct line shapes in the SC state for the three cases, a peak structure in the T dependence of T_1^{-1} can be found for all of them just below T_c as a result of the van Hove singularity, even though the SC gap has nodes. The effects of magnetic vortices on the low-energy excitations and on the T dependence of T_1^{-1} with the implications of the results are also discussed for all the cases.

DOI: 10.1103/PhysRevB.106.014501

I. INTRODUCTION

Recently, much attention has been focused on superconductivity in a family of compounds AV_3Sb_5 (A=K, Rb, and Cs) [1–35], which share a common lattice structure with a kagome net of vanadium atoms. Materials based on kagome lattices have been predicted to host exotic quantum physics because they embrace the geometrical lattice frustration, the flat electronic bands, the Dirac cones, and the topologically nontrivial surface states. Meanwhile, the superconducting (SC) phase appears next to a charge-density wave phase in the pressure-temperature phase diagram. As the electrons in these materials suffer simultaneously from the geometrical frustration, topological band structure, and the competition between different possible ground states, the observations of the superconductivity in these topological metals are in themselves exotic and rare. The connection to the underlying lattice geometry and the topological nature of the band structure further place them in the context of wider research efforts in topological physics and superconductivity.

To understand the underlying mechanism of the superconductivity in kagome superconductors and its connection to the lattice geometry and the topological nature of the band structure, numerous experiments with various means have been conducted in the past 2 yr. However, inconsistent or even contradicting results were found so far in experimental measurements and data analysis. The temperature dependence of the nuclear spin-lattice relaxation rate shows a Hebel-Slichter coherence peak just below T_c, indicating that CsV_3Sb_5 is a nodeless s-wave superconductor [14]. The penetration depth measurements also claim a nodeless gap [15]. Nevertheless, recent measurements of thermal conductivity on CsV_3Sb_5 at ultralow temperature evidenced a finite residual linear term, pointing to an unconventional nodal SC gap [16]. In accordance with this, the V-shaped SC gaps with residual zero-energy density of states (DOS) also suggest an anisotropic SC gap with nodes [11–13]. Moreover, the STM experiment on CsV_3Sb_5 at ultralow temperature revealed a two-gap structure with multiple sets of coherent peaks and residual zero-energy DOS, accompanied by the magnetic/nonmagnetic impurity effect, implying a rather novel and interesting SC gap, i.e., the sign preserved multiband superconductivity with gap nodes [12].

On the theoretical side, the vicinity to the van Hove filling was proposed to be crucial to the superconductivity on the kagome lattice. By using the variational cluster approach (VCA), the chiral ($d_{x^2-y^2} + id_{xy}$)-wave SC state was found to be the most favorable within a reasonable parameter range for the van Hove filling kagome system based on the single-orbital Hubbard model at 1/6 hole doping [36]. Moreover, in Ref. [36], the sublattice character of the Bloch state on the Fermi surface (FS) was shown to play a vital role in determining the superconductivity of the kagome system, which was also emphasized in the subsequent functional renormalization group (FRG) studies [37–39]. By considering the extended short-range interactions, the FRG studies on kagome systems discovered a rich variety of electron instability, including magnetism, charge order, as well as superconductivity near the van Hove filling [37–39]. More recently, a random-phase approximation based on a two-orbital model revealed a f-wave pairing instability over a large range of coupling

---

[*] monsoonjhm@sina.com
[†] slyu@nju.edu.cn
[‡] panxiaoyin@nbu.edu.cn

strength, succeeded by d-wave singlet pairing for stronger coupling [40]. Based on the kagome-lattice Hubbard model, the determinant quantum Monte Carlo calculations found the dominating pairing channel was the $(d_{x^2-y^2}+id_{xy})$ (s_{ex})-wave in the hole- (electron-) doped case [41]. Furthermore, it has been shown that the coexistence of time-reversal symmetry breaking with a conventional fully gapped superconductivity could lead to the gapless excitations on the domains of the lattice symmetry-breaking order [42]. The chiral flux phase has also been proposed to explain time-reversal symmetry breaking in the kagome superconductors [43,44].

In view of the divergent experimental observations and the various theoretical predictions, it is highly demanded to compare the consequences of the theoretical predictions on the experimental observations, especially with the emphases on the roles played by the van Hove singularity and the inequivalent bonds on the kagome lattice in a single-orbital Hubbard description. In this paper, we carry out such an investigation on the SC pairing symmetries of the kagome superconductors and compare their consequences on the experimental observations. The paper is to some extent an extension to Ref. [36] by incorporation of the three inequivalent third-neighbor (TN) bonds on the kagome lattice. Starting from a single-orbital tight-binding model on the kagome lattice near the van Hove singularity at 1/6 hole doping, the mean-field calculations demonstrate that the most favorable SC pairings are derived from the electrons belonging to the same sublattice sites, including the on-site s-wave and the spin-singlet/spin-triplet TN pairings, which are in line with the VCA results [36]. However, the incorporation of the inequivalent TN bonds will lead to the SC pairing possessing multiple components of orbital angular momentum (OAM) with mixed $[s_{ex}+(d\pm id')/(p\pm ip')+f]$-wave symmetries and, thus, contributes to the two-gap structures of the DOS. Although the spin-lattice relaxation exhibits distinct T dependence for the three cases, the Hebel-Slichter (or Hebel-Slichter-like) peak structure can be found for all of them just below T_c due to the Fermi level being near the van Hove singularity. In the vortex states, the cases for the on-site s-wave and the mixed $[s_{ex}+(d\pm id')]$-wave pairings possess discrete in-gap state peaks, located on either side of the zero energy. Nevertheless, the near-zero-energy in-gap state peak occurs in the vortex core for the case of the mixed $[(p\pm ip')+f]$-wave pairing. The vortices suppress the Hebel-Slichter (or Hebel-Slichter-like) peaks of the spin-lattice relaxation rate but enhance it at low temperature. Whereas a sophisticated multiorbital model is more appropriate to make a direct comparison to the experimental results, the multiple components of the SC pairing originated from the inequivalent bonds on the kagome lattice and the Hebel-Slichter (or Hebel-Slichter-like) peak of T_1^{-1} below T_c due to the vicinity of the van Hove filling are expected to persist in a realistic multiorbital description and should be reflected in the experimental observations, provided that the system situates close to the van Hove filling and the SC pairing is nonlocal.

The remainder of the paper is organized as follows. In Sec. II, we introduce the model Hamiltonian and carry out analytical calculations. In Sec. III, we present numerical calculations and discuss the results. In Sec. IV, we make a conclusion.

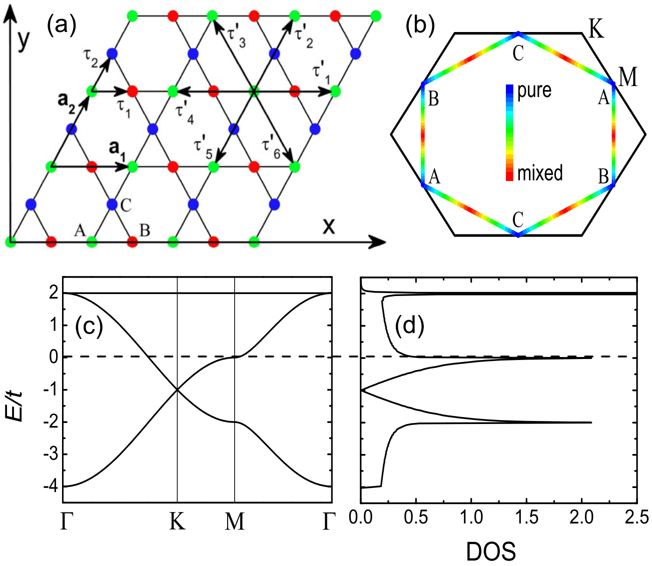

FIG. 1. (a) The lattice structure of the kagome superconductors made out of three sublattices A (green dots), B (red dots), and C (blue dots). $\mathbf{a_1}$ and $\mathbf{a_2}$ are two translational vectors, τ_1 and τ_2 are the nearest-neighbor vectors, and τ'_1-τ'_6 are the third-neighbor vectors. (b) Fermi surface and weights of the contribution to the Fermi surface from three inequivalent lattice sites A, B, and C as represented by the colors. (c) The tight-binding dispersion along high-symmetry cuts. The dashed line is the Fermi level corresponding to the van Hove filling. (d) Density of states for the normal state.

II. MODEL AND METHOD

The effective electron hoppings on a kagome lattice can be described by the following tight-binding Hamiltonian:

$$H_0 = -\sum_{\langle ij\rangle\sigma}(t_{ij}c^\dagger_{i\sigma}c_{j\sigma}+\text{H.c.})-\mu\sum_{i\sigma}c^\dagger_{i\sigma}c_{i\sigma}, \qquad (1)$$

where $c^\dagger_{i\sigma}$ creates an electron with spin σ on site $\mathbf{r}_i$ of the kagome lattice and $\langle ij\rangle$ denotes nearest-neighbors (NNs). t_{ij} is the hopping integral between the NN sites, and μ is the chemical potential. For the free hopping case with $t_{ij}=t$ at $\mu=0$, the Hamiltonian H_0 can be written in the momentum space,

$$H_0(k)=\sum_{k\sigma}\Psi^\dagger_{k\sigma}\mathcal{H}^0_k\Psi_{k\sigma}, \qquad (2)$$

with $\Psi_{k\sigma}=(c_{Ak\sigma},c_{Bk\sigma},c_{Ck\sigma})^T$ and

$$\mathcal{H}^0_k=-2t\begin{pmatrix}0 & \cos k_1 & \cos k_2\\ \cos k_1 & 0 & \cos k_3\\ \cos k_2 & \cos k_3 & 0\end{pmatrix}. \qquad (3)$$

The index $m=A,B,C$ in $c_{mk\sigma}$ labels the three basis sites in the triangular unit cell. k_n is abbreviated from $\mathbf{k}\cdot\tau_n$ with $\tau_1=\hat{x}/2$, $\tau_2=(\hat{x}+\sqrt{3}\hat{y})/4$, and $\tau_3=\tau_2-\tau_1$ denoting the three NN vectors. The label of the sublattice sites, the NN vectors, and the translational vectors are shown in Fig. 1(a). As shown in Fig. 1(c), the spectrum of $\mathcal{H}^0_k$ consists of one flat band $E^{(3)}_k=2t$ and two dispersive bands,

$$E^{(1,2)}_k=t(-1\pm\sqrt{4P_k-3}), \qquad (4)$$

with $P_k = \cos^2 k_1 + \cos^2 k_2 + \cos^2 k_3$. In addition to the two inequivalent Dirac points formed by the touching points of band 1 and 2 at $\mathbf{K}_\pm = (\pm 4\pi/3, 0)$ and the touching point of bands 2 and 3 at the center of the Brillouin zone (BZ) [45], there are three van Hove singularities with one originating from the flat band, and the other two originating from the saddle points at M points of the BZ as illustrated in Fig. 1(d). The Fermi levels at upper and lower saddle points correspond to the $1/6$ and $1/2$ hole dopings. Near the van Hove singularity at $1/6$ hole doping, the hexagonal FS shown in Fig. 1(b) bears much resemblance to the angle-resolved photoemission spectroscopy experimental observation and the density functional theory calculations [1], although a simple d-orbital tight-binding model is adopted. In the calculations, we focus our paper on the $1/6$ hole doping as has been performed in Ref. [36].

The SC pairing is assumed to derive from the effective attractions between electrons,

$$H_P = V \sum_{ij,\sigma\sigma'} n_{i,\sigma} n_{j,\sigma'}. \tag{5}$$

These effectively attractive interactions can be generated in a system with only local repulsive interactions through the Kohn-Luttinger mechanism [46], which was also supported by various numerical calculations beyond the mean-field theory, such as the VCA and the FRG in the Hubbard models on the kagome lattice near the van Hove filling [36,38]. The VCA and the FRG calculations have also shown that the nonlocal superconducting pairing caused by renormalized interaction was mainly on the TN bond, which links the sites in the same sublattice. On the other hand, the electron-phonon couplings may also be the possible origin of the effective attractive interactions. For example, near the van Hove singularity, the in-plane acoustic phonon modes have been proposed to mediate the effective SC pairing attraction between the sites in the same sublattice in the moiréless ABC-stacked rhombohedral trilayer graphene [47].

In the mean-field approximation, the attractions can lead to the SC pairings in the spin-singlet and spin-triplet channels, respectively, as

$$H_{Ps} = \sum_{ij} (\Delta_{s,ij} c^\dagger_{i,\uparrow} c^\dagger_{j,\downarrow} + \text{H.c.}), \tag{6}$$

and

$$H_{Pt} = \sum_{ij} (\Delta_{t,ij} c^\dagger_{i,\uparrow} c^\dagger_{j,\downarrow} + \text{H.c.}), \tag{7}$$

where the spin-singlet/-triplet pairing potential is defined as $\Delta_{s/t,ij} = \frac{V_{s/t}}{2}(\langle c_{i,\uparrow} c_{j,\downarrow}\rangle \mp \langle c_{i,\downarrow} c_{j,\uparrow}\rangle)$. On one hand, there is no experimental evidence of the preferred spin quantization axis in the SC state. On the other hand, since we do not include the spin-orbital coupling in the model, the spin configuration of the Cooper pairs does not affect our theoretical results. Thus, we consider the case of spin-triplet pairing with the **d** vector along the z axis for definiteness. Then, one obtains the total Hamiltonian as

$$H = H_0 + H_{Ps/t}. \tag{8}$$

Based on the Bogoliubov transformation, the diagonalization of the Hamiltonian H can be achieved by solving the following discrete Bogoliubov–de Gennes equations:

$$\sum_j \begin{pmatrix} H_{ij,\sigma} & \Delta_{s/t,ij} \\ \Delta^*_{s/t,ij} & -H^*_{ij,\bar{\sigma}} \end{pmatrix} \begin{pmatrix} u_{n,j,\sigma} \\ v_{n,j,\bar{\sigma}} \end{pmatrix} = E_n \begin{pmatrix} u_{n,i,\sigma} \\ v_{n,i,\bar{\sigma}} \end{pmatrix}, \tag{9}$$

where $H_{ij,\sigma} = -t_{ij}\delta_{i+\tau_j,j} - \mu\delta_{i,j}$ with τ_j denoting the four NN vectors. $u_{n,i,\sigma}$ and $v_{n,i,\bar{\sigma}}$ are the Bogoliubov quasiparticle amplitudes on the ith site with corresponding eigenvalue E_n. The SC pairing amplitudes and electron densities are obtained through the following self-consistent equations:

$$\begin{aligned} \Delta_{s/t,ij} &= \frac{V_{s/t}}{4} \sum_n (u_{n,i,\sigma} v^*_{n,j,\bar{\sigma}} \pm v^*_{n,i,\bar{\sigma}} u_{n,j,\sigma}) \\ &\quad \times \tanh\left(\frac{E_n}{2k_B T}\right) \\ n_{i,\uparrow} &= \sum_n |u_{n,i,\uparrow}|^2 f(E_n) \\ n_{i,\downarrow} &= \sum_n |v_{n,i,\downarrow}|^2 [1 - f(E_n)]. \end{aligned} \tag{10}$$

III. RESULTS AND DISCUSSION

In the self-consistent calculations, the chemical potential μ is tuned so as to fix the band filling at $1/6$ hole doping. At $1/6$ hole doping since the van Hove singularity at each saddle-point M on the FS comes only from one of the three inequivalent lattice sites as shown in Fig. 1(b), one can expect that the favorable Cooper pairing in the mean-field level is derived from two electrons belonging to the same sublattice, i.e., the on-site or the TN-site pairing, which is in accordance with the VCA and the FRG calculations [36,38]. Although there are some mixing contributions away from the M points and the NN or second NN pairing length is shorter than the TN pairing, the low DOS renders the intersublattice pairings unfavorable at the mean-field level. We also check the cases of the intersublattice pairings, including the NN and the second NN pairings, and find that their amplitudes are negligible in the reasonable parameter ranges. Therefore, we consider the on-site and the TN pairings in the following.

For the kagome lattice, there are six TNs for each lattice site, and they give rise to three inequivalent bonds as denoted by τ'_1, τ'_2, and τ'_3 in Fig. 1(a). Whereas only spin-singlet pairing is allowed for the on-site pairing, both the spin-singlet and spin-triplet pairings are permissible for the TN bonds. Since the three bonds are different, we only set the pairing on each bond to be spin singlet or spin triplet, and let the pairing amplitude on the three different bonds to be determined self-consistently. For the TN pairings, we have $\Delta_{s/t,\tau'_4} = \pm\Delta_{s/t,\tau'_1}$, $\Delta_{s/t,\tau'_5} = \pm\Delta_{s/t,\tau'_2}$, and $\Delta_{s/t,\tau'_6} = \pm\Delta_{s/t,\tau'_3}$ for the spin-singlet/spin-triplet pairings. In the calculations, we choose the typical values of the effective pairing interactions $V_s = V_{s0} = 1.6$ for the on-site s-wave pairing, $V_s = V_{s1} = 1.2$ for the TN spin-singlet pairing, and $V_t = 1.4$ for the TN spin-triplet pairing, respectively, to give rise to the comparable SC transition temperatures for the three cases. Varying these parameters will change the pairing amplitude,

TABLE I. Pairing strength on the three inequivalent TN bonds for the three sublattice sites.

		$\Delta_{s/t,\tau_1'}$	$\Delta_{s/t,\tau_2'}$	$\Delta_{s/t,\tau_3'}$
TN spin-singlet	*A* site	0.05	0.05	−0.03
	B site	0.05	−0.03	0.05
	C site	−0.03	0.05	0.05
TN spin-triplet	*A* site	−0.04	0.04	−0.067
	B site	−0.04	0.067	−0.04
	C site	−0.067	0.04	−0.04

and, thus, the SC transition temperature. Nevertheless, the mixed pairings with their relative mixing strengths remain unchanged upon the variation of these parameters, and accordingly the other results will be qualitatively robust against the different pairing interaction strengths.

At zero field, the self-consistent results of the TN pairing amplitudes on the three different bonds around three sublattice sites are displayed in Table I. The different pairing strengths on the three inequivalent bonds within each sublattice will generally lead to a SC pairing with multiple components of OAM. From the perspective of the point symmetry, the kagome lattice is described by C_{6v} point-group symmetry. Accordingly, the possible pairing states can be classified, in principle, by the irreducible representations of C_{6v}. Whereas s_{ex}-wave and f-wave pairing states correspond to one-dimensional representation A_1, $(d \pm id')$-wave and $(p \pm ip')$-wave belong to two-dimensional representations E_2 and E_1, respectively. Nevertheless, each sublattice has only the C_{2v} symmetry due to the three inequivalent TN bonds (intrasublattice bonds). Under the operations of the point-group C_{2v}, the s_{ex}- and d-wave pairing states behave exactly the same and so is the p- and f-wave pairing states (see Fig. 2 in Ref. [36] for a reference). This is to say that the s_{ex} wave (p wave) and d wave (f wave) in each sublattice with the C_{2v} symmetry belong to the equivalent representation. Thus, one can expect that the mixture of different pairing states occurs on the NN bond of each sublattice (the TN bond of the kagome lattice), which is verified by the self-consistent results shown in Tables I and II. On the other hand, the pairings on the three sublattices A, B, and C are precisely related by the C_6 rotational symmetry as displayed in Table I. Therefore, if we consider the SC pairings on the three sublattices simultaneously, the C_6 rotational symmetry is restored, being consistent with the requirement of the C_{6v} symmetry of the whole system.

TABLE II. Pairing amplitude for the different OAM components.

	$\Delta_0^{s_{ex}/f}$	$\Delta_0^{d+id'/p+ip'}$	$\Delta_0^{d-id'/p-ip'}$
TN spin-singlet	0.023	0.027	0.027
TN spin-triplet	0.049	0.009	0.009

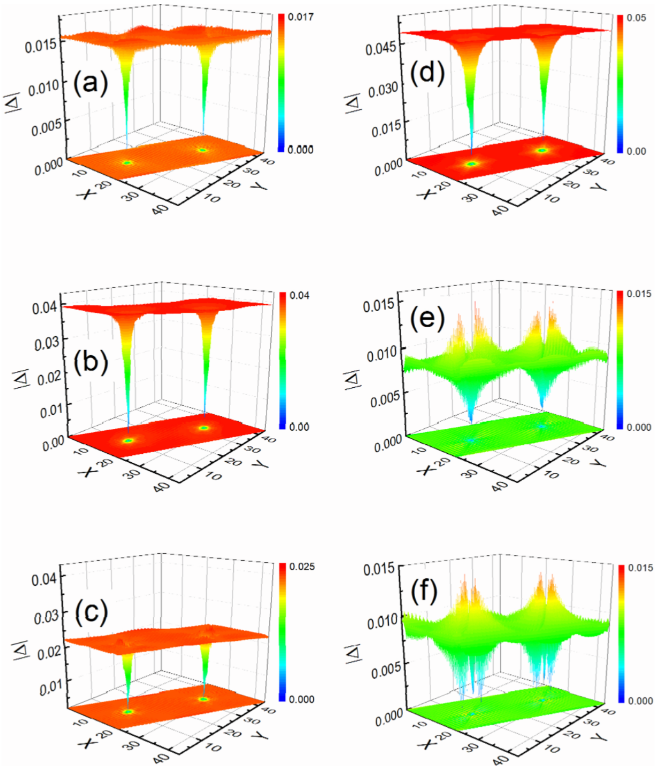

FIG. 2. The spatial distributions of the SC order parameters in the vortex states for the mixed $[s_{ex} + (d \pm id')]$- (left panel), and $[(p \pm ip') + f]$-wave (right panel) symmetries. (a)–(c) show the spatial distributions of the amplitudes for the s_{ex}, $d + id'$, and $d - id'$ components, respectively. (d)–(f) show the spatial distributions of the amplitudes for the f, $p + ip'$, and $p - ip'$ components, respectively.

It would be useful to gain a better understanding of the symmetries of the TN bond SC pairings in the kagome lattice from the real-space description. In real space, the pairing amplitude on site $\mathbf{r}_i$ is generally defined as

$$\Delta^{l}_{s/t,\pm}(\mathbf{r}_i) = \frac{1}{N_c} \sum_{\tau_j'} \Delta_{s/t,\tau_j'} e^{il\theta_{\pm}(\tau_j')}. \tag{11}$$

Here, $\Delta^{l}_{s/t,\pm}(\mathbf{r}_i)$ stands for the clockwise/anticlockwise ($\pm$) spin-singlet/-triplet (s/t) pairing with OAM l in units of $\hbar$, which determines the spatial symmetry of the Cooper pair wave function. $\theta_{\pm}(\tau_j')$ denotes the polar angle of the TN bond measured clockwise/anticlockwise from the x axis, and N_c is the number of the TN site around $\mathbf{r}_i$. In Eq. (11), $\Delta^{l}_{s/t,\pm}(\mathbf{r}_i)$ with $l = 0$–$3\cdots$ picks up, respectively, the OAMs of $s, p, d, f\cdots$ waves, and the relationship between $\Delta^{l}_{s/t,+}(\mathbf{r}_i)$ and $\Delta^{l}_{s/t,-}(\mathbf{r}_i)$ tells us the information about the pairing chirality. From Eq. (11) and the self-consistent results shown in Table I, one could get mixed $[s_{ex} + (d \pm id')]$-wave symmetry for the TN spin-singlet pairing and mixed $[(p \pm ip') + f]$-wave symmetry for the TN spin-triplet pairing. Although the $(d \pm id')$- and $(p \pm ip')$-wave components fall into a category of topological ones characterized, respectively, by the integer winding numbers (Chern number) $C = \mp 2$ and $C = \pm 1$, the s_{ex}- and f-wave components are topologically trivial with $C = 0$. The mixing of them produces the SC states with the topological properties depending on the relative weight of the components. At one extreme, i.e., the $(d \pm id')$-wave [$(p \pm ip')$-wave] component has the dominant weight, the mixed $[s_{ex} + (d \pm id')]$-wave

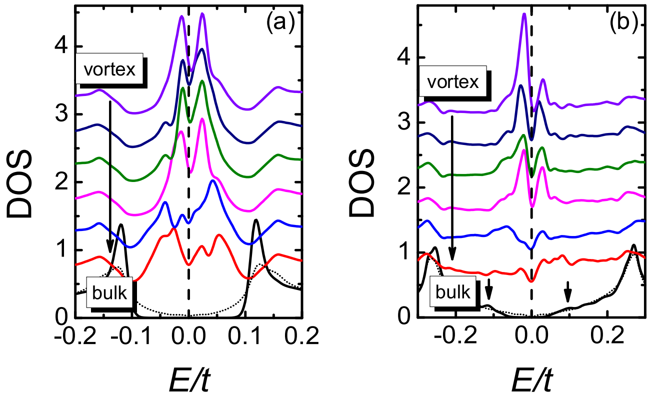

FIG. 3. The energy dependence of the LDOS on a series of sites for (a) on-site spin-singlet pairing, (b) spin-singlet pairing on the TN bond, and (c) spin-triplet pairing on the TN bond. In each panel from top to bottom, the curves stand for the LDOS at sites along the long side direction of the parallelogram moving away from the core center. The curves are vertically shifted for clarity. At the bottom of each panels, the site-averaged DOSs in the uniform SC state and in the vortex states are plotted as solid black lines and dotted black lines, respectively. The dashed vertical lines in each panel denote the position of the zero bias, and the short arrows in (b) and (c) mark the secondary gap edges.

$[(p \pm ip') + f]$-wave SC state remains the same topological property as the $(d \pm id')$-wave $(p \pm ip')$-wave pairing. At the other extreme, the mixed SC states become topologically trivial ones. Despite maintaining the nonzero Chern number, the situations in between could be topologically trivial in terms of the absence of the gapless states on the edge or in the vortex core, much like the proposals of the fragile topological phase [48–54].

In reciprocal space, the components with different OAMs have the following form:

$$\begin{aligned}
\Delta_{s_{ex}}(\mathbf{k}) &= \Delta_0^{s_{ex}}[\cos(k_x) + 2\cos(k_x/2)\cos(\sqrt{3}k_y/2)],\\
\Delta_{d\pm id'}(\mathbf{k}) &= \Delta_0^{d\pm id'}[\cos(k_x) - \cos(k_x/2)\cos(\sqrt{3}k_y/2)\\
&\quad \pm i\sqrt{3}\sin(k_x/2)\sin(\sqrt{3}k_y/2)],\\
\Delta_{p\pm ip'}(\mathbf{k}) &= \Delta_0^{p\pm ip'}[\sin(k_x) + \sin(k_x/2)\cos(\sqrt{3}k_y/2)\\
&\quad \pm i\sqrt{3}\cos(k_x/2)\sin(\sqrt{3}k_y/2)],\\
\Delta_f(\mathbf{k}) &= \Delta_0^f[\sin(k_x) - 2\sin(k_x/2)\cos(\sqrt{3}k_y/2)], \quad (12)
\end{aligned}$$

where $\Delta_0^{s_{ex}} = |\Delta_s^0|$, $\Delta_0^{d\pm id'} = |\Delta_{s,\pm}^2|$, $\Delta_0^{p\pm ip'} = |\Delta_{t,\pm}^1|$, and $\Delta_0^f = |\Delta_t^3|$. The values of the s_{ex}/f-wave components $\Delta_0^{s_{ex}}/\Delta_0^f$ and the $[d \pm id'/p \pm ip']$-wave components $\Delta_0^{d\pm id'}/\Delta_0^{p\pm ip'}$ are shown in Table II, and the sign distributions of the pairing components refer to Ref. [36] for details. Whereas the s_{ex}- and $d \pm id'$-wave components exhibit comparable strength for the TN spin-singlet pairing, the f-wave component dominates over the $(p \pm ip')$-wave component for the TN spin-triplet pairing. The smallness of the $(p \pm ip')$-wave component in the mixed $[(p \pm ip') + f]$-wave symmetry pairing state will not remove the nodes of the f-wave pairing but will move them, resulting in an unusual SC pairing state with accidental nodes. The equality of $\Delta_0^{d+id'/p+ip'}$ and $\Delta_0^{d-id'/p-ip'}$ dictates the two degenerate SC pairing states with right and left chiralities in the $[d \pm id'/p \pm ip']$-wave component at zero field.

The three typical SC pairings in their uniform SC states produce distinct site-averaged DOS spectra $N(E) = \frac{1}{N}\sum_i N(E,\mathbf{r}_i)$ with definition $N(E,\mathbf{r}_i) = N_\uparrow(E,\mathbf{r}_i) + N_\downarrow(E,\mathbf{r}_i) = -\sum_n[|u^n_{i,\uparrow}|^2 f'(E_n - E) + |v^n_{i,\downarrow}|^2 f'(E_n + E)]$, which is proportional to the differential tunneling conductance observed in scanning tunneling microscopy (STM) experiments. The results are summarized by the solid black lines at the bottom of each panels in Fig. 3. For the on-site s-wave symmetry, a single U-shaped full gap structure can be seen in the DOS as shown by the solid black line in Fig. 3(a), depicting a typical feature of the isotropic SC gap without nodes along the FS. In the $[s_{ex} + (d \pm id')]$-wave symmetry, the DOS consists of a small U-shaped gap structure at low energy and a broad V-shaped gap structure at higher energy as shown in Fig. 3(b), presenting an anisotropic nodeless two-gap structure. As for the $[(p \pm ip') + f]$-wave symmetry shown in Fig. 3(c), dominant f-wave component plus a tiny value of $(p \pm ip')$-wave component produce a broad V-shaped gap structure inlaid by a small V-shaped gap with residual DOS at zero energy in the SC state, displaying a characteristic of nodal two-gap SC pairing. We note that the V-shaped SC gap with multiple sets of coherent peaks and residual zero-energy DOS are in good accordance with the STM experiments [11–13].

Now we address the vortex structure of the three types of the SC states. In the presence of a perpendicular magnetic field, the hopping terms are described by the Peierls substitution. For the NN hopping between sites i and $i + \tau_j$, one has $t_{i,i+\tau_j} = te^{i\varphi_{i,i+\tau_j}}$, where $\varphi_{i,i+\tau_j(\tau_j')} = \frac{\pi}{\Phi_0}\int_{r_{i+\tau_j(\tau_j')}}^{r_i}\mathbf{A}(\mathbf{r})\cdot d\mathbf{r}$ with $\Phi_0 = \frac{hc}{2e}$ being the SC flux quanta. In this case, the pairing amplitude on site $\mathbf{r}_i$ is reformulated as $\Delta^l_{s/t,\pm}(\mathbf{r}_i) = \frac{1}{N_c}\sum_{\tau_j'}\Delta_{s/t,\tau_j'}e^{il\theta_\pm(\tau_j')}e^{i\varphi_{i,i+\tau_j'}}$ for the TN bond pairings. In the calculations, we consider a parallelogram vortex unit cell with size of $22\mathbf{a_1} \times 44\mathbf{a_2}$ as shown in Fig. 1(a) where two vortices are accommodated. The vector potential $\mathbf{A}(\mathbf{r}) = (0, Bx, 0)$ is chosen in the Landau gauge to give rise to the magnetic-field $\mathbf{B}$ along the z direction.

Under a perpendicular magnetic field, the vanishment of the screening current density at the vortex center drives the system into the vortex states with the suppression of the SC order parameter around the vortex core, thereby forming a vortex with winding +1. In the vortex states, the SC order parameter $|\Delta(\mathbf{r}_i)|$ vanishes at the vortex core center and recovers its bulk value at the core edge with the core size ξ_1 on the scale of coherent length ξ as can be seen from Fig. 2 for two cases. (The result of the on-site s-wave pairing is similar and not shown here.) Besides the standard SC vortex structure, there are two prominent features to be specified in the vortex states for the SC pairings with multiple OAM components on the kagome lattice. First, consistent with the STM experimental observations in $\mathrm{CsV_3Sb_5}$ [12] and similar to the observations in $\mathrm{NbSe_2}$ [55–57] and $\mathrm{YNi_2B_2C}$ [58–60], the vortex core has a typical star shape with sixfold symmetry for the three cases, reflecting the underlying crystalline band structure. Second, the aforementioned two degenerate SC pairing states with right and left chiralities for the $(d \pm id'/p \pm ip')$-wave components are removed under a perpendicular magnetic field because $(d \pm id'/p \pm ip')$-wave components correspond to states with an internal phase winding of the Cooper pairs along the z axis. In the mixed $[s_{ex} + (d \pm id')]$-wave pairing state, the comparable strength for the s_{ex}- and $[d \pm id']$-wave components renders both of them to response effectively to the magnetic field. The internal phase of the $(d + id')$-wave component has a −2 winding, which counteracts the phase winding +1 of the vortex to save the energy cost of supercurrents. As a result, the application of the magnetic field transfers the weight from the s_{ex}- and $(d - id')$-wave components to the $(d + id')$-wave component in the mixed $[s_{ex} + (d \pm id')]$-wave pairing state as evidenced by a comparison of Table II with the spatial distributions of the SC order parameters in Figs. 2(a)–(c). On the other hand, the screening current density from the dominant f-wave component in the mixed $[(p \pm ip') + f]$-wave symmetry pairing diminishes the impact of the magnetic field on the $(p \pm ip')$-wave components, so there is a little degeneracy lifting for the two chiral $(p \pm ip')$-wave components as shown in Figs. 2(e) and 2(f), despite the $(p - ip')$-wave component possessing the internal phase winding −1.

Then, we pursuit the electronic structures in the vortex states by examining the energy dependence of the local DOS (LDOS). In order to reduce the finite-size effect, the calculations of the LDOS are carried out on a periodic lattice which consists of 16 × 8 parallelogram supercells with each supercell being the size $22\mathbf{a_1} \times 44\mathbf{a_2}$. In Fig. 3, we show the energy dependence of the LDOS on a series of sites along the long side direction of the parallelogram moving away from the core center. Since both the on-site s-wave and the mixed $[s_{ex} + (d \pm id')]$-wave pairings are fully gaped, similar in-gap states appear in the core region. At the vortex center, the Caroli–de Gennes–Matricon states accumulate to give rise to two peaks reside on each side about the zero energy, forming a small gap at the zero energy. As the site moving away from the vortex center, the two peaks depart further and fade away as presented in Figs. 3(a) and 3(b). For the mixed $[(p \pm ip') + f]$-wave symmetry pairing, by contrast, a near-zero-energy peak appears at the vortex center, which does not disperse in a long distance as moving away from the vortex center. It is worth noting that the near-zero-energy peak and the dispersionless of the peak are again in excellent agreement with the STM experimental observations [13]. It should also be noted that the near-zero-energy peak structure has a usual origin as expected from the nodal SC state with the lowest vortex bound state lying close to zero energy [61], instead of the topologically protected gapless states, such as the Majorana zero modes.

Next, we turn to the discussion of the T dependence of T_1^{-1}. The site-dependent $T_1^{-1}(\mathbf{r}_i, \mathbf{r}_{i'})$ is given by [62,63]

$$\begin{aligned} R(\mathbf{r}_i, \mathbf{r}_{i'}) &= \mathrm{Im}\, \chi_{\pm}(\mathbf{r}_i, \mathbf{r}_{i'}, i\Omega_n \to \Omega + i\eta)/(\Omega/T)|_{\Omega\to 0} \\ &= -\sum_{n,n'} [u_{n,i} u^*_{n,i'} v_{n',i} v^*_{n',i'} - v_{n,i} u^*_{n,i'} u_{n',i} v^*_{n',i'}] \\ &\quad \times \pi T f'(E_n) \delta(E_n - E_{n'}). \end{aligned} \tag{13}$$

We choose $\mathbf{r}_i = \mathbf{r}_{i'}$ because the nuclear spin-lattice relaxation at a local site is dominant. Then the site-dependent relaxation time is given by $T_1(\mathbf{r}_i) = 1/R(\mathbf{r}_i, \mathbf{r}_i)$ and the bulk relaxation time $T_1 = (1/N) \sum_i T_1(\mathbf{r}_i)$. In the calculations, we adopt $\delta(E_n - E_{n'}) = \pi^{-1} \mathrm{Im}(E_n - E_{n'} - i\eta)^{-1}$ with a typical value of $\eta = 0.01$. In a conventional s-wave superconductor, the T dependence of T_1^{-1} develops a peak structure below T_c, which is called the Hebel-Slichter coherent peak as observed experimentally in SC Al by Hebel and Slichter [64] and explained theoretically as a result of the enhancement of the SC DOS at the gap edge along with the nonzero coherent factor described in BCS theory [64]. Thus, the observation of the Hebel-Slichter peak below T_c is usually considered to be the hallmark of s-wave superconductivity [14].

In the absence of the magnetic field, the Hebel-Slichter (or Hebel-Slichter-like) peaks of T_1^{-1} below T_c are evidenced in Figs. 4(a)–(c) for the three cases. It is quite remarkable for the case of the mixed $[(p \pm ip') + f]$-wave with a nodal SC gap. To figure out the origin as well as the different nature of the peaks, we show in the same figures the T evolution of $R_D \equiv -\frac{1}{N} \sum_{i,n,n'} (u_{n,i} u^*_{n,i'} v_{n',i} v^*_{n',i'}) \pi T f'(E_n) \delta(E_n - E_{n'})$ and $R_C \equiv \frac{1}{N} \sum_{n,n'} (v_{n,i} u^*_{n,i'} u_{n',i} v^*_{n',i'}) \pi T f'(E_n) \delta(E_n - E_{n'})$, i.e., the contributions from the first and second terms in Eq. (13) to T_1^{-1}. R_D is proportional to $N_\uparrow N_\downarrow$, which gives rise to the enhancement of the SC DOS at the gap edge with the enhancement depending upon the sharpness of the SC gap edge and the specific DOS of the normal state on where the SC gap opens. On the other hand, R_C describes the coherent effect of the SC state. As seen in Fig. 4(c) and the insets of Figs. 4(a) and 4(b), the T evolutions of R_D develop a peak just below T_c for the three cases (note that only R_D contributes to T_1^{-1} and, accordingly, $R_D = T_1^{-1}$ for the mixed $[(p \pm ip') + f]$-wave pairing as will be shown in the following) due to the fact that the infinitesimal SC gaps opening at the van Hove singularity with divergent DOS would also have divergent DOSs at the gap edges. However, the T dependence of R_C is different for the three cases. Specifically, R_C evolves a peak below T_c for the cases of the on-site s- and the mixed $[s_{ex} + (d \pm id')]$-wave symmetries, whereas it remains zero for the case of the mixed $[(p \pm ip') + f]$-wave symmetry. This can be understood by noting that the mixed triplet $[(p \pm ip') + f]$-wave pairing with odd parity $\Delta_{ji} = -\Delta_{ij}$ forbids the local SC correlation $u_{n,i} v^*_{n,i}$.

Thus far, we have demonstrated that the results for the mixed $[(p \pm ip') + f]$-wave symmetry reconcile the various inconsistent or apparently contradicting experiments, includ-

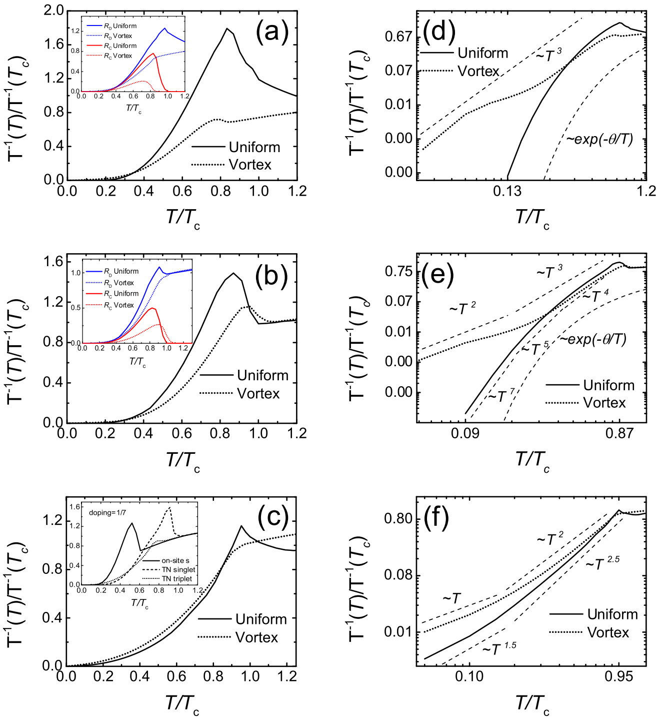

FIG. 4. Left panels: T dependence of T_1^{-1}. Right panels: T dependence of T_1^{-1} shown in the double logarithmic chart. (a) and (d) show the results for the on-site pairing, (b) and (e) the results for the spin-singlet pairing on the TN bond, and (c) and (f) the results for the spin-triplet pairing on the TN bond. The insets in (a) and (b) display the T evolutions of R_D and R_C (see the text). The inset in (c) gives the results of T dependence of T_1^{-1} for the three cases at doping 1/7.

ing the V-shaped SC gap with residual DOS at zero energy, the dispersionless of the near-zero energy peak in the vortex core, as well as the Hebel-Slichter-like peak of the T dependence of T_1^{-1}. Whereas the appearance of the Hebel-Slichter-like peak for the mixed $[(p \pm ip') + f]$-wave symmetry here seems to support the nuclear magnetic resonance (NMR) experiment, its origin is different in nature from the Hebel-Slichter coherent peak. The Hebel-Slichter coherent peak for the on-site s- and the mixed $[s_{ex} + (d \pm id')]$-wave pairing symmetries derives from the simultaneous enhancement of R_D and R_c, but the peak for the case of the mixed $[(p \pm ip') + f]$-wave symmetry originates merely from the enhancement of R_D. Due to the nodal SC gap of the mixed $[(p \pm ip') + f]$-wave pairing, the sharpness of the SC gap edge is weakened as the Fermi level deviating from the van Hove singularity, and this, in turn, undermines the Hebel-Slichter-like peak. As a result, the Hebel-Slichter-like peak for the case of the mixed $[(p \pm ip') + f]$-wave symmetry diminishes and eventually disappears with the Fermi-level deviation from the van Hove filling. This is verified in the inset of Fig. 4(c) for a specified doping level 1/7. By contrast, the Hebel-Slichter peak remains robust for the cases of the on-site s- and the mixed $[s_{ex} + (d \pm id')]$-wave pairing symmetries. To verify or falsify the above scenario, the NMR experiments on different doping levels, especially on situations with the Fermi level being far from the van Hove singularity [22,65], are encouraged to observe the doping evolutions of the Hebel-Slichter-like peak.

Below T_c, the three cases, however, exhibit distinct T dependence of T_1^{-1}. The on-site s-wave pairing evolves into an exponential dependence below T_c as presented by the solid line in Fig. 4(d), which is the consequence of the full-gaped DOS in Fig. 3(a). The gap anisotropy of the mixed $[s_{ex} + (d \pm id')]$-wave pairing changes the exponential dependence to a power-law relation $T_1^{-1} \sim T^{\alpha}$ with α varying from 4 to 5 below T_c and $T_1^{-1} \sim T^7$ at low temperature as displayed by the solid line in Fig. 4(e). For the case of $[(p \pm ip') + f]$-wave symmetry pairing, the T dependence of T_1^{-1} changes its line shape further to $T_1^{-1} \sim T^{2.5}$ below T_c and $T_1^{-1} \sim T^{1.5}$ at low temperature, shown in Fig. 4(f), as a result of the V-shaped gap and the residual DOS at zero energy.

In the presence of the perpendicular magnetic field, on one hand, the intensity of the Hebel-Slichter (or Hebel-Slichter-like) peaks are suppressed by localized excitations within the vortex cores [62,66]. Whereas strong depression of the peak of R_C below T_c can be seen for the case of the on-site s-wave pairing [see the inset of Fig. 4(a)], the depression is just moderate with the peak position shifting slightly toward higher temperature for the mixed $[s_{ex} + (d \pm id')]$-wave pairing symmetry [the inset of Fig. 4(b)], owing to the offsetting effect of the internal phase of the $(d + id')$-wave component [see Fig. 2(b)]. As a result, one could barely see a trail of the peak as shown by the dotted black line in Fig. 4(a) for the on-site s-wave pairing symmetry, but still evidence a robust peak feature with its position moving slightly to higher temperature for the mixed $[s_{ex} + (d \pm id')]$-wave pairing symmetry [refer to the dotted black line in Fig. 4(b)]. Nevertheless, the peak of R_D below T_c is suppressed completely for all the cases due to the blunting of the gap edges as shown by the dotted black lines in Figs. 3(a)–(c). This directly leads to the disappearance of the Hebel-Slichter-like peak for the case of the mixed $[(p \pm ip') + f]$-wave symmetry as presented by the dotted line in Fig. 4(c). On the other hand, the main effect of the vortices is to enhance the T dependence of T_1^{-1} for all symmetries at low temperature. The enhancement of T_1^{-1} is exemplified in Fig. 4(d) by changing the exponential T dependence to roughly T^3 below T_c, despite little variations, for the on-site s-wave symmetry. Due to the anisotropic SC gap for the mixed $[s_{ex} + (d \pm id')]$-wave pairing symmetry and the nodal SC gap for the mixed $[(p \pm ip') + f]$-wave symmetry [see the dotted black lines in Figs. 3(b) and 3(c)], the enhancement becomes more pronounced in a T^{β} power law below T_c and $T^{\beta-1}$ at lower temperature with $\beta = 3$ for the mixed $[s_{ex} + (d \pm id')]$-wave pairing symmetry and $\beta = 2$ for the the mixed $[(p \pm ip') + f]$-wave symmetry as denoted by the dotted lines in Figs. 4(e) and 4(f), respectively.

IV. CONCLUSION

To summarize, we have carried out a contrastive study on the kagome superconductors at the van Hove filling with the incorporation of the inequivalent TN bonds. Although the most favorable SC pairings were derived from the electrons belonging to the same sublattice sites, the consideration of the inequivalent TN bonds would result in the SC pairings with multiple OAM components and, thus, contributed to the two-gap structures of the DOS. Whereas the T_1^{-1} exhibited distinct T dependence in the SC state for the three cases, a peak structure has been found for all of them just below T_c. Unlike the coherent peak for the cases of the on-site s- and the mixed $[s_{ex} + (d \pm id')]$-wave pairings, which was derived from both the enhancement of the SC DOS at the gap edge and the nonzero SC coherent effect, the van Hove singularity was crucial to the peak in the mixed $[(p \pm ip') + f]$-wave pairing, where only the enhancement of the SC DOS at the gap edge contributed to the peak structure. In the vortex states, the cases for the on-site s-wave and the mixed $[s_{ex} + (d \pm id')]$-wave pairings created discrete in-gap state peaks, which located on either side of the zero energy. By contrast, the near-zero-energy and almost dispersionless in-gap state peaks occurred in the vortex core for the case of the mixed $[(p \pm ip') + f]$-wave pairing. Whereas the vortices diminished the Hebel-Slichter (or Hebel-Slichter-like) peaks and enhanced the T dependence of T_1^{-1} in the SC state for all the cases, the T dependencies of T_1^{-1} were also distinct with respect to the different gap functions. Whereas a more sophisticated multiorbital model is needed to make a direct comparison to the experimental results, the SC pairing with multiple OAM components originated from the inequivalent bonds on the kagome lattice and the Hebel-Slichter (or Hebel-Slichter-like) peak of T_1^{-1} below T_c due to the vicinity of the van Hove filling were expected to persist in a realistic multiorbital description and should be reflected in the experimental observations, provided that the system situated close to the van Hove filling and the SC pairing was nonlocal. The NMR experiments on different doping levels and on the T dependence of the T_1^{-1} in the SC state both with and without a perpendicular magnetic field were expected to testify the theory.

Note added. After completion of this paper, we become aware of recent interesting study on the vortex states in the kagome superconductors by using the similar tight-binding model [67]. The SC vortex was simulated in Ref. [67] by setting the spatial-dependent pairing amplitude $\Delta(\mathbf{r}_i) = \Delta \tanh(\frac{\mathbf{r}_i}{\xi})$, whereas the results in our paper were determined self-consistently.

ACKNOWLEDGMENTS

We thank Professor J.-X. Li for fruitful discussions and valuable suggestions. This work was supported by the National Natural Science Foundation of China (Grants No. 11574069 and No. 12074175) and the K. C. Wong Magna Foundation in Ningbo University.

---

[1] B. R. Ortiz, S. M. L. Teicher, Y. Hu, J. L. Zuo, P. M. Sarte, E. C. Schueller, A. M. M. Abeykoon, M. J. Krogstad, S. Rosenkranz, R. Osborn, R. Seshadri, L. Balents, J. He, and S. D. Wilson, Phys. Rev. Lett. **125**, 247002 (2020).

[2] B. R. Ortiz, P. M. Sarte, E. M. Kenney, M. J. Graf, S. M. L. Teicher, R. Seshadri, and S. D. Wilson, Phys. Rev. Materials **5**, 034801 (2021).

[3] Q. Yin, Z. Tu, C. Gong, Y. Fu, S. Yan, and H. Lei, Chin. Phys. Lett. **38**, 037403 (2021).

[4] K. Y. Chen, N. N. Wang, Q. W. Yin, Y. H. Gu, K. Jiang, Z. J. Tu, C. S. Gong, Y. Uwatoko, J. P. Sun, H. C. Lei, J. P. Hu, and J.-G. Cheng, Phys. Rev. Lett. **126**, 247001 (2021).

[5] Y. Wang, S. Yang, P. K. Sivakumar, B. R. Ortiz, S. M. L. Teicher, H. Wu, A. K. Srivastava, C. Garg, D. Liu, S. S. P. Parkin, E. S. Toberer, T. McQueen, S. D. Wilson, and M. N. Ali, arXiv:2012.05898.

[6] Z. Zhang, Z. Chen, Y. Zhou, Y. Yuan, S. Wang, J. Wang, H. Yang, C. An, L. Zhang, X. Zhu, Y. Zhou, X. Chen, J. Zhou, and Z. Yang, Phys. Rev. B **103**, 224513 (2021).

[7] Y.-X. Jiang, J.-X. Yin, M. M. Denner, N. Shumiya, B. R. Ortiz, G. Xu, Z. Guguchia, J. He, M. S. Hossain, X. Liu, J. Ruff, L. Kautzsch, S. S. Zhang, G. Chang, I. Belopolski, Q. Zhang, T. A. Cochran, D. Multer, M. Litskevich, Z.-J. Cheng *et al.*, Nature Mater. **20**, 1353 (2021).

[8] F. H. Yu, T. Wu, Z. Y. Wang, B. Lei, W. Z. Zhuo, J. J. Ying, and X. H. Chen, Phys. Rev. B **104**, L041103 (2021).

[9] X. Chen, X. Zhan, X. Wang, J. Deng, X.-B. Liu, X. Chen, J.-G. Guo, and X. Chen, Chin. Phys. Lett. **38**, 057402 (2021).

[10] H. Zhao, H. Li, B. R. Ortiz, S. M. L. Teicher, T. Park, M. Ye, Z. Wang, L. Balents, S. D. Wilson, and I. Zeljkovic, Nature (London) **599**, 216 (2021).

[11] H. Chen, H. Yang, B. Hu, Z. Zhao, J. Yuan, Y. Xing, G. Qian, Z. Huang, G. Li, Y. Ye, S. Ma, S. Ni, H. Zhang, Q. Yin, C. Gong, Z. Tu, H. Lei, H. Tan, S. Zhou, C. Shen *et al.*, Nature (London) **599**, 222 (2021).

[12] H.-S. Xu, Y.-J. Yan, R. Yin, W. Xia, S. Fang, Z. Chen, Y. Li, W. Yang, Y. Guo, and D.-L. Feng, Phys. Rev. Lett. **127**, 187004 (2021).

[13] Z. Liang, X. Hou, F. Zhang, W. Ma, P. Wu, Z. Zhang, F. Yu, J.-J. Ying, K. Jiang, L. Shan, Z. Wang, and X.-H. Chen, Phys. Rev. X **11**, 031026 (2021).

[14] C. Mu, Q. Yin, Z. Tu, C. Gong, H. Lei, Z. Li, and J. Luo, Chin. Phys. Lett. **38**, 077402 (2021).

[15] W. Duan, Z. Nie, S. Luo, F. Yu, B. R. Ortiz, L. Yin, H. Su, F. Du, A. Wang, Y. Chen, X. Lu, J. Ying, S. D. Wilson, X. Chen, Y. Song, and H. Yuan, Sci. China: Phys., Mech. Astron. **64**, 107462 (2021).

[16] C. C. Zhao, L. S. Wang, W. Xia, Q. W. Yin, J. M. Ni, Y. Y. Huang, C. P. Tu, Z. C. Tao, Z. J. Tu, C. S. Gong, H. C. Lei, Y. F. Guo, X. F. Yang, and S. Y. Li, arXiv:2102.08356.

[17] S. Ni, S. Ma, Y. Zhang, J. Yuan, H. Yang, Z. Lu, N. Wang, J. Sun, Z. Zhao, D. Li, S. Liu, H. Zhang, H. Chen, K. Jin, J. Cheng, L. Yu, F. Zhou, X. Dong, J. Hu, H.-J. Gao *et al.*, Chin. Phys. Lett. **38**, 057403 (2021).

[18] Y. Xiang, Q. Li, Y. Li, W. Xie, H. Yang, Z. Wang, Y. Yao, and H.-H. Wen, Nat. Commun. **12**, 6727 (2021).

[19] B. R. Ortiz, S. M. L. Teicher, L. Kautzsch, P. M. Sarte, N. Ratcliff, J. Harter, J. P. C. Ruff, R. Seshadri, and S. D. Wilson, Phys. Rev. X **11**, 041030 (2021).

[20] X. Zhou, Y. Li, X. Fan, J. Hao, Y. Dai, Z. Wang, Y. Yao, and H.-H. Wen, Phys. Rev. B **104**, L041101 (2021).

[21] Z. Liu, N. Zhao, Q. Yin, C. Gong, Z. Tu, M. Li, W. Song, Z. Liu, D. Shen, Y. Huang, K. Liu, H. Lei, and S. Wang, Phys. Rev. X **11**, 041010 (2021).

[22] M. Kang, S. Fang, J.-K. Kim, B. R. Ortiz, S. H. Ryu, J. Kim, J. Yoo, G. Sangiovanni, D. D. Sante, B.-G. Park, C. Jozwiak, A.

Bostwick, E. Rotenberg, E. Kaxiras, S. D. Wilson, J.-H. Park, and R. Comin, Nat. Phys. **18**, 301 (2022).

[23] Y. Fu, N. Zhao, Z. Chen, Q. Yin, Z. Tu, C. Gong, C. Xi, X. Zhu, Y. Sun, K. Liu, and H. Lei, Phys. Rev. Lett. **127**, 207002 (2021).

[24] Y. Song, T. Ying, X. Chen, X. Han, X. Wu, A. P. Schnyder, Y. Huang, J.-g. Guo, and X. Chen, Phys. Rev. Lett. **127**, 237001 (2021).

[25] H. Tan, Y. Liu, Z. Wang, and B. Yan, Phys. Rev. Lett. **127**, 046401 (2021).

[26] N. Shumiya, Md. S. Hossain, J.-X. Yin, Y.-X. Jiang, B. R. Ortiz, H. Liu, Y. Shi, Q. Yin, H. Lei, S. S. Zhang, G. Chang, Q. Zhang, T. A. Cochran, D. Multer, M. Litskevich, Z.-J. Cheng, X. P. Yang, Z. Guguchia, S. D. Wilson, and M. Z. Hasan, Phys. Rev. B **104**, 035131 (2021).

[27] F. H. Yu, D. H. Ma, W. Z. Zhuo, S. Q. Liu, X. K. Wen, B. Lei, J. J. Ying, and X. H. Chen, Nat. Commun. **12**, 3645 (2021).

[28] L. Yin, D. Zhang, C. Chen, G. Ye, F. Yu, B. R. Ortiz, S. Luo, W. Duan, H. Su, J. Ying, S. D. Wilson, X. Chen, H. Yuan, Y. Song, and X. Lu, Phys. Rev. B **104**, 174507 (2021).

[29] K. Nakayama, Y. Li, T. Kato, M. Liu, Z. Wang, T. Takahashi, Y. Yao, and T. Sato, Phys. Rev. B **104**, L161112 (2021).

[30] K. Jiang, T. Wu, J.-X. Yin, Z. Wang, M. Z. Hasan, S. D. Wilson, X. Chen, and J. Hu, arXiv:2109.10809.

[31] L. Nie, K. Sun, W. Ma, D. Song, L. Zheng, Z. Liang, P. Wu, F. Yu, J. Li, M. Shan, D. Zhao, S. Li, B. Kang, Z. Wu, Y. Zhou, K. Liu, Z. Xiang, J. Ying, Z. Wang, T. Wu *et al.*, Nature (London) **604**, 59 (2022).

[32] H. Luo, Q. Gao, H. Liu, Y. Gu, D. Wu, C. Yi, J. Jia, S. Wu, X. Luo, Y. Xu, L. Zhao, Q. Wang, H. Mao, G. Liu, Z. Zhu, Y. Shi, K. Jiang, J. Hu, Z. Xu, and X. J. Zhou, Nat. Commun. **13**, 273 (2022).

[33] T. Neupert, M. M. Denner, J.-X. Yin, R. Thomale, and M. Z. Hasan, Nat. Phys. **18**, 137 (2022).

[34] K. Nakayama, Y. Li, T. Kato, M. Liu, Z. Wang, T. Takahashi, Y. Yao, and T. Sato, Phys. Rev. X **12**, 011001 (2022).

[35] H. Li, S. Wan, H. Li, Q. Li, Q. Gu, H. Yang, Y. Li, Z. Wang, Y. Yao, and H.-H. Wen, Phys. Rev. B **105**, 045102 (2022).

[36] S.-L. Yu and J.-X. Li, Phys. Rev. B **85**, 144402 (2012).

[37] M. L. Kiesel and R. Thomale, Phys. Rev. B **86**, 121105(R) (2012).

[38] W.-S. Wang, Z.-Z. Li, Y.-Y. Xiang, and Q.-H. Wang, Phys. Rev. B **87**, 115135 (2013).

[39] M. L. Kiesel, C. Platt, and R. Thomale, Phys. Rev. Lett. **110**, 126405 (2013).

[40] X. Wu, T. Schwemmer, T. Müller, A. Consiglio, G. Sangiovanni, D. Di Sante, Y. Iqbal, W. Hanke, A. P. Schnyder, M. M. Denner, M. H. Fischer, T. Neupert, and R. Thomale, Phys. Rev. Lett. **127**, 177001 (2021).

[41] C. Wen, X. Zhu, Z. Xiao, N. Hao, R. Mondaini, H.-M. Guo, and S. Feng, Phys. Rev. B **105**, 075118 (2022).

[42] Y. Gu, Y. Zhang, X. Feng, K. Jiang, and J. Hu, Phys. Rev. B **105**, L100502 (2022).

[43] X. Feng, K. Jiang, Z. Wang, and J. Hu, Sci. Bull. **66**, 1384 (2021).

[44] X. Feng, Y. Zhang, K. Jiang, and J. Hu, Phys. Rev. B **104**, 165136 (2021).

[45] H.-M. Guo and M. Franz, Phys. Rev. B **80**, 113102 (2009).

[46] W. Kohn and J. M. Luttinger, Phys. Rev. Lett. **15**, 524 (1965).

[47] Y.-Z. Chou, F. Wu, J. D. Sau, and S. Das Sarma, Phys. Rev. Lett. **127**, 187001 (2021).

[48] H. C. Po, H. Watanabe, and A. Vishwanath, Phys. Rev. Lett. **121**, 126402 (2018).

[49] J. Cano, B. Bradlyn, Z. Wang, L. Elcoro, M. G. Vergniory, C. Felser, M. I. Aroyo, and B. A. Bernevig, Phys. Rev. Lett. **120**, 266401 (2018).

[50] A. Alexandradinata, J. Höller, C. Wang, H. Cheng, and L. Lu, Phys. Rev. B **102**, 115117 (2020).

[51] Z.-D. Song, L. Elcoro, Y.-F. Xu, N. Regnault, and B. A. Bernevig, Phys. Rev. X **10**, 031001 (2020).

[52] Y. Hwang, J. Ahn, and B.-J. Yang, Phys. Rev. B **100**, 205126 (2019).

[53] Z.-D. Song, L. Elcoro, and B. A. Bernevig, Science **367**, 794 (2020).

[54] V. Peri, Z.-D. Song, M. Serra-Garcia, P. Engeler, R. Queiroz, X. Huang, W. Deng, Z. Liu, B. A. Bernevig, and S. D. Huber, Science **367**, 797 (2020).

[55] H. F. Hess, R. B. Robinson, and J. V. Waszczak, Phys. Rev. Lett. **64**, 2711 (1990).

[56] N. Hayashi, M. Ichioka, and K. Machida, Phys. Rev. Lett. **77**, 4074 (1996).

[57] N. Hayashi, M. Ichioka, and K. Machida, Phys. Rev. B **56**, 9052 (1997).

[58] H. Nishimori, K. Uchiyama, S. Kaneko, A. Tokura, H. Takeya, K. Hirata, and N. Nishida, J. Phys. Soc. Jpn. **73**, 3247 (2004).

[59] Y. Nagai, Y. Kato, N. Hayashi, K. Yamauchi, and H. Harima, Phys. Rev. B **76**, 214514 (2007).

[60] S. Kaneko, K. Matsuba, M. Hafiz, K. Yamasaki, E. Kalizaki, N. Nishida, H. Takeya, K. Hirata, T. Kawakami, T. Mizushima, and K. Machida, J. Phys. Soc. Jpn. **81**, 063701 (2012).

[61] Y. Wang and A. H. MacDonald, Phys. Rev. B **52**, R3876(R) (1995).

[62] M. Takigawa, M. Ichioka, and K. Machida, Phys. Rev. Lett. **83**, 3057 (1999); **90**, 047001 (2003); M. Takigawa, M. Ichioka, K. Kuroki, Y. Asano, and Y. Tanaka, *ibid.* **97**, 187002 (2006).

[63] H.-M. Jiang, J. Guo, and J.-X. Li, Phys. Rev. B **84**, 014533 (2011).

[64] L. C. Hebel and C. P. Slichter, Phys. Rev. **113**, 1504 (1959).

[65] Y. Hu, X. Wu, B. R. Ortiz, S. Ju, X. Han, J. Ma, N. C. Plumb, M. Radovic, R. Thomale, S. D. Wilson, A. P. Schnyder, and M. Shi, Nat. Commun. **13**, 2220 (2022).

[66] N. J. Curro, Rep. Prog. Phys. **72**, 026502 (2009).

[67] P. Ding, C. H. Lee, X. Wu, and R. Thomale, Phys. Rev. B **105**, 174518 (2022).